scientific reports

OPEN

Impacts of plasmonic nanoparticles incorporation and interface energy alignment for highly efficient carbon-based perovskite solar cells

MirKazem Omrani[1✉], Reza Keshavarzi[2✉], Mojtaba Abdi-Jalebi[3✉] & Peng Gao[4✉]

This work utilizes a realistic electro-optical coupled simulation to study the (i) impact of mesoporous TiO$_2$ removal; (ii) the embedding of Ag@SiO$_2$ and SiO$_2$@Ag@SiO$_2$ plasmonic nanoparticles; (iii) utilization of solution-processed inorganic p-type copper(I) thiocyanate (CuSCN) layer at the perovskite/carbon interface; and (iv) the increase of the work function of carbon electrodes (via incorporation of suitable additives/binders to the carbon ink) on the performance of carbon-based PSCs. Removal of mesoporous TiO$_2$ increased the power conversion efficiency (PCE) of the device from 14.83 to 16.50% due to the increase in exciton generation rate and charge carriers' mobility in the vicinity of the perovskite-compact TiO$_2$ interface. Subsequently, variable mass ratios of Ag@SiO$_2$ and SiO$_2$@Ag@SiO$_2$ plasmonic nanoparticles are embedded in the vicinity of the perovskite-compact TiO$_2$ interface. In the optimum cases, the PCE of the devices increased to 19.72% and 18.92%, respectively, due to light trapping, scattering, and strong plasmonic fields produced by the plasmonic nanoparticles. Furthermore, adding the CuSCN layer remarkably increased the PCE of the device with a 0.93% mass ratio of Ag@SiO$_2$ nanoparticles from 19.72 to 26.58% by a significant improvement of V$_{oc}$ and FF, due to the proper interfacial energy band alignment and the reduction of the recombination current density. Similar results were obtained by increasing the carbon work function, and the cell PCE was enhanced up to 26% in the optimal scenario. Our results pave the way to achieve high efficiencies in remarkably stable printable carbon-based PSCs.

Over the past decade, perovskite solar cells have become a promising candidate as a future source of energy. The unique optical and electrical properties of perovskites, such as high absorption coefficient, direct bandgap, long carrier diffusion length, and low exciton binding energy, have led to rapid growth and a significant increase in the device efficiency from 3.8 to > 25%[1,2]. However, most of the high-efficiency perovskite solar cells are fabricated with expensive organic materials (e.g., 2,2′,7,7′-tetrakis-(*N*,*N*-di-4-methoxyphenylamino)-9,9′-spirobifluorene (spiro-OMeTAD)) as the hole transfer layer (HTL) and noble metal (e.g., Au) as the electrode, which is deposited by thermal evaporation in a vacuum environment. This not only increases the cost of production but also reduces the stability of the device due to the degradation because of the mobile behavior of Au contact at 70 °C and the poor stability of Spiro-OMeTAD[3,4].

In recent years, HTL-free carbon-based perovskite solar cells have attracted much academic and industrial attention for their outstanding stability with lower production costs[5–12]. In this case, when a carbon-based material is replaced with the metal contact and the HTL, the non-encapsulated device exhibits excellent stability in an ambient environment[13]. However, the efficiency of carbon-based devices is significantly lower than their counterparts equipped with HTL/metal back contact, where the highest efficiency of HTL-free carbon-based perovskite solar cells is ~ 15%[14].

In general, the interface of the perovskite photoactive layer and the electron transfer layer (ETL) (which often includes the compact and mesoporous TiO$_2$) plays a crucial role in achieving high efficiency[15,16]. The mesoporous structure acts as a pathway for electron transfer by increasing the contact surface between the perovskite and

[1]Department of Physics, University of Isfahan, 81746-73441 Isfahan, Iran. [2]Department of Chemistry, Catalysis Division, University of Isfahan, 81746-73441 Isfahan, Iran. [3]Institute for Materials Discovery, University College London, Malet Place, London WC1E 7JE, UK. [4]Xiamen Key Laboratory of Rare Earth Photoelectric Functional Materials, Fujian Institute of Research On the Structure of Matter, Chinese Academy of Sciences, Xiamen 361021, Fujian, People's Republic of China. ✉email: kazem.omrani@semnan.ac.ir; r.keshavarzi@chem.ui.ac.ir; m.jalebi@ucl.ac.uk; peng.gao@firsm.ac.cn
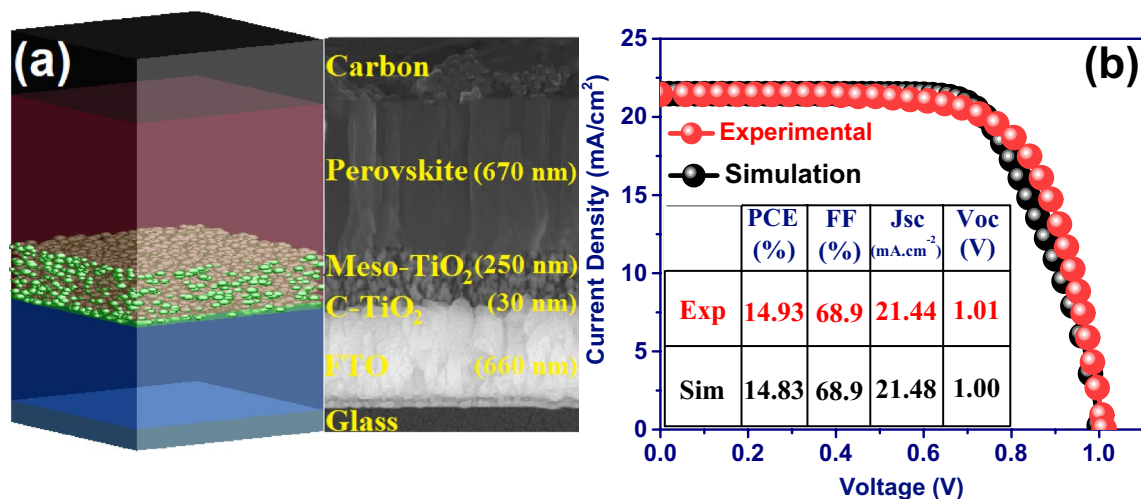
Figure 1. (**a**) Device configuration used for simulation and cross-section image of the experimental HTL-free carbon-based perovskite solar cell. (**b**) The photocurrent density–voltage (J-V) curves from experimental and simulation validation of the perovskite solar cell. J-V characteristics of the devices have been measured under one sun simulated illumination.

TiO_2 [17]. However, the presence of isolated TiO_2 nanoparticles can lead to charge accumulation and increased recombination due to the trapping of electron carriers and the low mobility of carriers in the perovskite-filled mesoporous structure. This, in turn, affects hysteresis behavior in measuring the efficiency and instability of the device due to the ion migration[18]. Therefore, providing a carbon-based planar structure by removing mesoporous TiO_2 can not only reduce the device's hysteresis behavior[19] but also take another step toward commercializing perovskite-based solar cells by reducing the cost of mass production.

One of the most effective approaches to increase the efficiency of carbon-based perovskite solar cells is to use plasmonic nanoparticles within the device structure[20–26]. Under light illumination, metal nanoparticles create strongly localized fields around them during the coherent oscillations of their conducting electrons[27,28], which can not only increase the photon flux inside the perovskite as a secondary light source but also increase the generation rate of free carriers by reducing the exciton binding energy[29]. In addition, the light scattering by resonated nanoparticles can increase the absorption via enlarging of the light pathway, even at thin perovskite thicknesses[30]. On the other hand, plasmonic nanoparticles generate hot electrons during plasmon resonance which can be directly injected into their surrounding perovskite environment and increase photo-generated electrons mobility by filling the trap states[31].

To take advantage of local surface plasmon resonance (LSPR) effects, metal nanoparticles must be added to the photoactive layer. First, however, a capping layer over the metallic nanoparticles must be used due to the corrosive properties of $CH_3NH_3PbI_3$, which lead to the decomposition of noble metals[32]. Then, heating the nanoparticles metallic surface during plasmon resonance will lead to the recombination of excitons at their surface[33]. Here, the usage of a thin layer of SiO_2 as a capping layer not only stabilizes the noble metal nanoparticles against thermal and chemical interactions but also creates the slightest manipulation in the LSPR properties of the nanoparticles[21]. The presence of a dielectric coating layer can attenuate the plasmonic properties of the nanoparticles. In some studies[21,34,35], to improve the plasmonic effects of nanoparticles, triple core–shell nanostructures with a metal nanoshell sandwiched between the dielectric outer shell and core (e.g. $SiO_2@Ag@SiO_2$ and $TiO_2@Au@TiO_2$) have been proposed, which can produce better LSPR properties thanks to their plasmon hybridization mechanism.

Herein, we improve the performance of HTL-free carbon-based planar perovskite solar cells using plasmonic NPs. Firstly, the photovoltaic measurements of the fabricated HTL-free carbon-based perovskite solar cell have been utilized for simulation and extract the electrical parameters via fitting its corresponding *J-V* characteristics. Then, a detailed analysis of the device performance in the presence of mesoporous TiO_2 and planar structure has been presented using electro-optical coupled simulation regimes. Next, the effect of realistic embedding of Ag@SiO_2 and $SiO_2@Ag@SiO_2$ nanoparticles with different concentrations on the optical and electrical performance of the carbon-based planar perovskite solar cell has been investigated. Finally, since the presence of a carbon electrode (work function of ~ 5 eV) as the non-ideal anode limits the device efficiency, for increasing the transfer rate of hole carriers and blocking the electron carriers, we investigate the effects of adding a copper(I) thiocyanate (CuSCN) interlayer at the perovskite-carbon interface and increasing the working function of carbon electrode on the performance of carbon-based perovskite solar cells.

Results and discussion

The structure of the fabricated and modeled device is Glass/FTO/Compact TiO_2/Mesoporous TiO_2/$CH_3NH_3PbI_3$/Carbon (see Fig. 1a). Here, the mesoporous TiO_2 is considered inside the perovskite photoactive layer. In other words, the pore sites of the mesoporous TiO_2 are filled with perovskite material. In the simulated structures, mesoporous TiO_2 is made of deformed TiO_2 nanospheres with a size distribution of 7–10 nm that can overlap
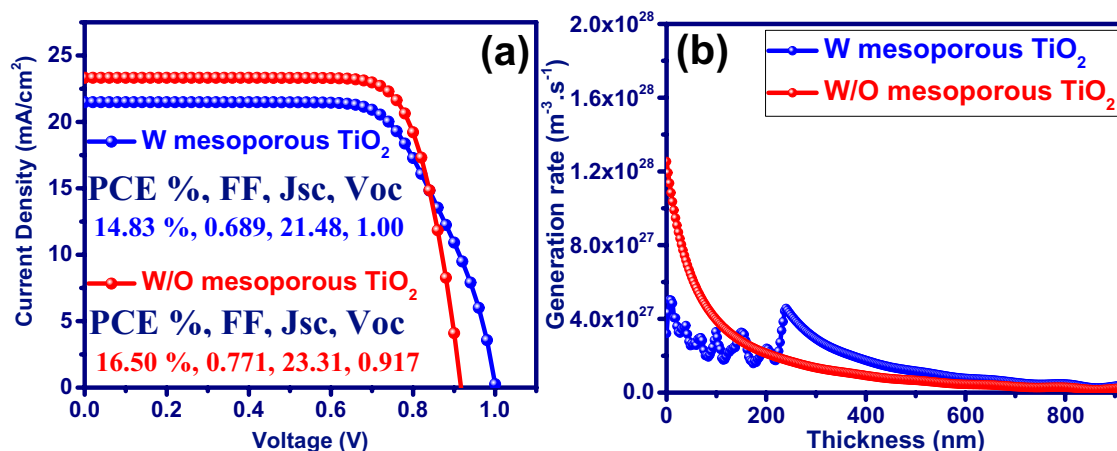
Figure 2. (**a**) J–V characteristics of the device and (**b**) Spatial profile of photo-generated charges in $CH_3NH_3PbI_3$ photoactive layer with (W) and without (W/O) incorporation of mesoporous TiO_2.

with each other and randomly distribute within an equivalent thickness of ~ 250 nm with a porosity of ~ 39% (Fig. 1a). This modeling is based on the results of FESEM and ellipsometry analyzes of the fabricated solar cell[40]. Accurate modeling of the structure of the mesoporous TiO_2 is crucial because it plays a vital role in the distribution of the field profile within the perovskite layer. This directly affects the exciton distribution, generation, and recombination rates of charge carriers along with the photoactive layer. Essential details considered in this modeling have not been reported in any of the previously published works.

Figure 1b shows the measured current–voltage curves from the experimental device compared to the simulation results, wherein the simulation results are in complete agreement with the experimental data. The power conversion efficiency (PCE) of 14.93% and 14.83% for the HTL-free carbon-based perovskite solar cell has been measured and obtained from the simulation, respectively. Furthermore, all the electrical characteristics obtained from the simulation (V_{oc}, J_{sc}, FF, and PCE) are in good agreement with the experimental data, which shows that the modeling performed in this work can explain the experimental optical-electrical characteristics. Therefore, it provides a good description of the device performance.

The first perovskite solar cell manufacture was based on dye-sensitized solar cells in which the TiO_2 mesoporous was used as the electron transfer layer. The main reason for using the mesoporous structure was to assume the short diffusion length of the carriers in the perovskite. Researchers later found that the perovskite diffusion length is at least more than 100 nm. Accordingly, TiO_2 mesoporous is removed from the device structure, and its effect on the performance of the solar cell is investigated in Fig. 2 using the developed modeling. Embedding the mesoporous TiO_2 in the perovskite-compact TiO_2 interface can reduce the mobility of charge carriers in this region. This is the reason for obtaining the low charge carriers mobility during the fitting of the simulation results with those of the experimental data (see Fig. 1b and Table S1). Removal of TiO_2 mesoporous has increased the power conversion efficiency (PCE) from 14.83 to 16.50% due to J_{sc} and FF improvement (Fig. 2a). Investigation of the exciton generation rate profile along the perovskite layer shows that the improved device performance is due to the increased exciton generation rate and charge carrier mobility near compact TiO_2 (Fig. 2b).

To benefit from the plasmonic properties of metallic nanoparticles in improving the performance of carbon-based planer perovskite solar cells, $Ag@SiO_2$ core–shell nanoparticles, and $SiO_2@Ag@SiO_2$ triple core–shell nanoparticles have been embedded at the interface of $CH_3NH_3PbI_3$-compact TiO_2 (Fig. 3). These plasmonic nanostructures have been designed and optimized in our previous studies and introduced as effective plasmonic nanoparticles[21]. Here, the deformed nanospheres capable of overlapping with each other are randomly distributed in a volumetric space with varying mass ratios (the volume of distributed plasmonic nanoparticles/perovskite layer volume × 100) using a realistic simulation. The overall dimensions of the nanoparticles, the thicknesses of Ag inner shell and SiO_2 outer shell are 32 nm, 2.5 nm, and 1 nm, respectively.

The device efficiency has increased to 19.72% and 18.20% after adding a 0.93% mass ratio of $Ag@SiO_2$ and $SiO_2@Ag@SiO_2$ NPs, respectively, due to the J_{sc} increment shown in Fig. 3. Further increment of the mass ratio of embedded $Ag@SiO_2$ nanoparticles decreases the efficiency stemming from the J_{sc} drop (Table 1). This could be due to the enhancement of the reflectivity behavior of nanoparticles, which prevents light from penetrating deep into the perovskite layer. This, in turn, can weaken the performance of the device by reducing the optical absorption. However, the increase in the mass ratio of $SiO_2@Ag@SiO_2$ nanoparticles has increased the device efficiency, and the maximum power conversion efficiency of 18.92% is obtained for the devices incorporated with the mass ratios of 2.79% (Fig. 3b and Table 1). Removal of mesoporous TiO_2 and adding 0.93% mass ratio of $Ag@SiO_2$ NPs between perovskite and compact-TiO_2 have increased the device efficiency by 33%. The presence of mesoporous TiO_2 and the addition of NPs within the mesoporous structure could only increase the device efficiency by 17% (Fig. 3c and Table 2). This suggests that the presence of TiO_2 mesoporous as the surrounding environment of doped plasmonic nanoparticles can weaken their plasmonic enhancement.

In Figs. 4 and 5, the LSPR properties of $SiO_2@Ag@SiO_2$ and $Ag@SiO_2$ nanoparticles embedded in the perovskite environment are investigated, respectively, as single-particle and mass during plasmon resonance. Compared
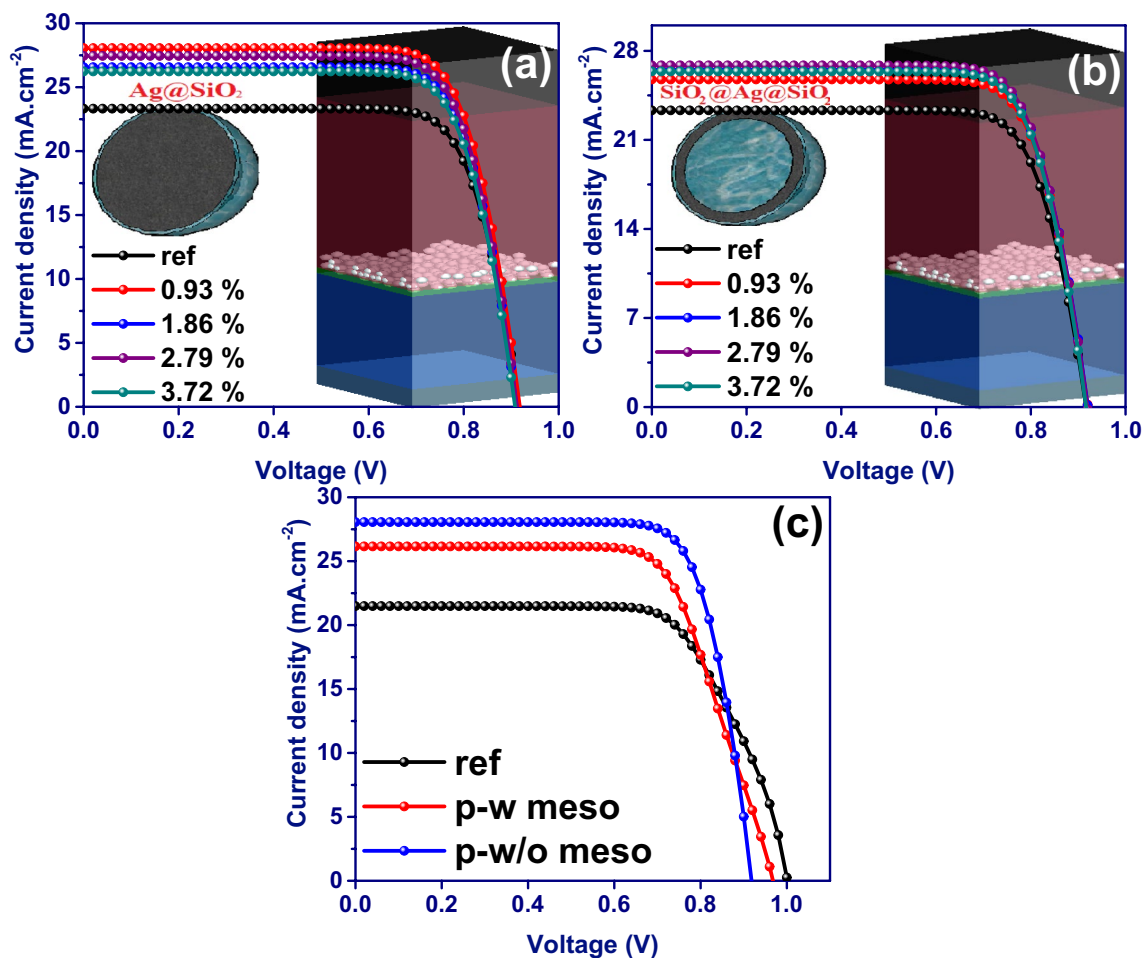
Figure 3. J-V characteristics of the incorporated planar devices with the different mass ratios of (**a**) $Ag@SiO_2$ and (**b**) $SiO_2@Ag@SiO_2$ nanospheres. (**c**) J–V characteristics of the device incorporated with a 0.93% mass ratio of $Ag@SiO_2$ NPs in the presence (p-w meso) and absence (p-w/o meso) of mesoporous TiO_2.

NPs	Samples	J_{sc} (mA/cm²)	V_{oc} (V)	FF (%)	PCE (%)
Ag@SiO₂	ref	23.31	0.917	77.10	16.50
	0.93	28.05	0.918	76.57	19.72
	1.86	26.56	0.911	76.65	18.55
	2.79	27.44	0.912	76.55	19.16
	3.72	26.23	0.908	76.66	18.26
SiO₂@Ag@SiO₂	ref	23.31	0.917	77.10	16.50
	0.93	25.74	0.920	76.86	18.20
	1.86	26.50	0.920	76.74	18.71
	2.79	26.85	0.919	76.68	18.92
	3.72	26.38	0.916	76.72	18.54

Table 1. Electrical characteristics of the simulated devices incorporated with $SiO_2@Ag@SiO_2$ and $Ag@SiO_2$ NPs with different mass ratios.

NPs	Samples	J_{sc} (mA/cm²)	V_{oc} (V)	FF (%)	PCE (%)
w/o doping	ref w meso	21.48	1.00	68.90	14.83
Ag@SiO₂ (0.93)	p-w meso	26.15	0.968	68.56	17.35
	p-w/o meso	28.05	0.918	76.57	19.72

Table 2. Electrical characteristics of the simulated device incorporated with a 0.93% mass ratio of $Ag@SiO_2$ NPs in the presence (p-w meso) and absence (p-w/o meso) of mesoporous TiO_2.
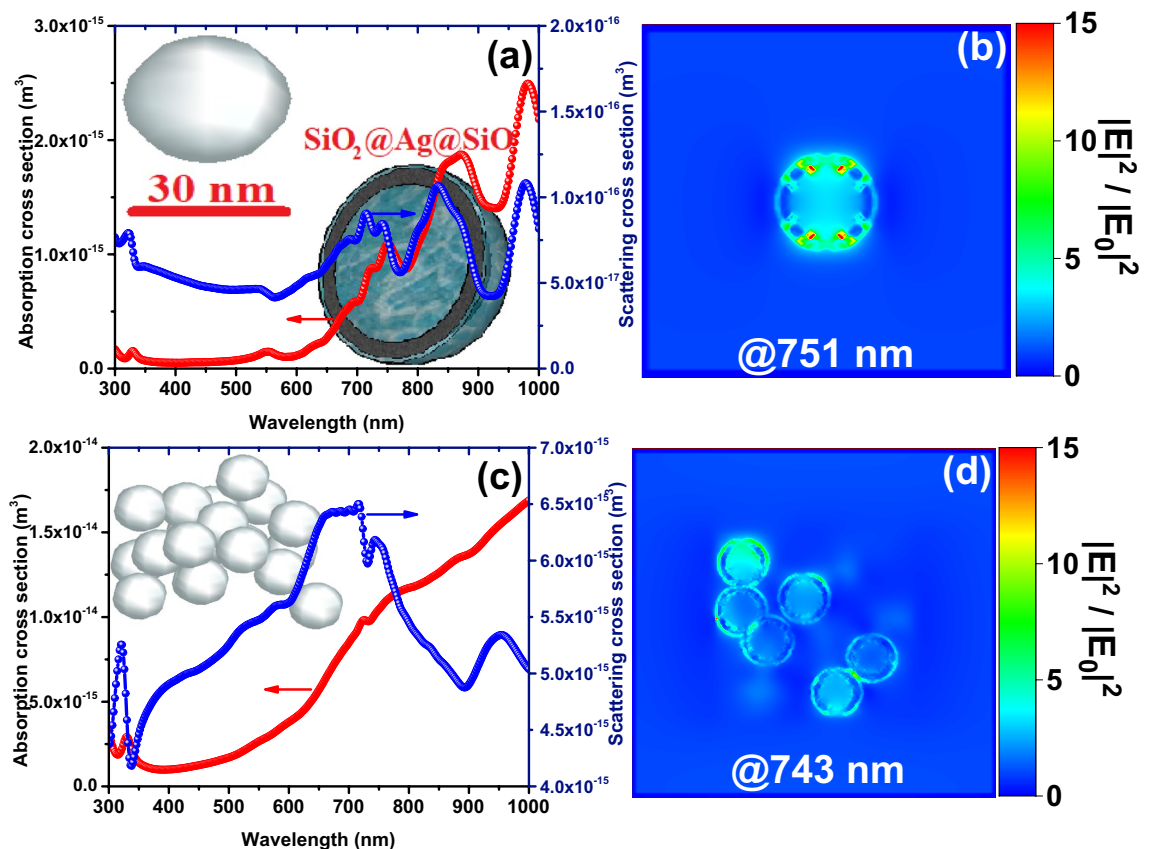
Figure 4. Absorption and scattering cross-sections (**a**, **c**) and near-field intensity enhancement (**b**, **d**) of (**a**, **b**) single and (**c**, **d**) a mass of 20 triple core–shell SiO_2@Ag@SiO_2 nanospheres (1 nm SiO_2 utter shell, 2.5 nm Ag inner shell and total size of 32 nm).

to the single nanoparticle, mass nanoparticles show a larger absorption cross-section due to the production of new plasmonic peaks and their increase in spectral width due to plasmonic interactions of neighboring nanoparticles (Fig. 4a and c). This is a reason for further improvement in the efficiency of the device incorporated with SiO_2@Ag@SiO_2 nanoparticles by increasing the mass ratio of embedded nanoparticles (Fig. 3b). Plasmon resonance of SiO_2@Ag@SiO_2 nanoparticles occurs due to the plasmon hybridization mechanism at higher wavelengths than Ag@SiO_2 nanoparticles (Figs. 4 and 5), where the photon flux produced by the nanoparticle is unable to transfer electrons from the valance band to the conduction band of perovskite. This results in less plasmonic improvement of the device in the presence of SiO_2@Ag@SiO_2 nanoparticles compared to Ag@SiO_2 nanoparticles. In addition, Ag@SiO_2 nanoparticles generate stronger plasmonic fields in the perovskite environment compared to SiO_2@Ag@SiO_2 nanoparticles. Figure S2 shows the absorption spectrum of perovskite in the presence of a 0.93% mass ratio of Ag@SiO_2 and SiO_2@Ag@SiO_2 nanoparticles compared to the reference device (without nanoparticles). As expected, perovskite absorption in the presence of Ag@SiO_2 nanoparticles shows further improvement.

The presence of a carbon electrode (work function of ~ 5 eV) as the non-ideal anode and the absence of an electron blocking layer at the perovskite-carbon interface limits the device efficiency by enhancing the probability of electron recombination at the interface. Adding an appropriate interlayer at the perovskite-carbon interface and/or adequate increment of the working function of carbon by using suitable additives/binders in carbon ink to increase the transfer rate of hole carriers while blocking electron carriers are other approaches to improve the performance of carbon-based perovskite solar cells. In metal electrode-based perovskite solar cells, spiro-OMeTAD has been widely used as a representative of hole transport material[41,42]. However, there are significant limitations to the use of this material (and generally organic and conductive polymer-based molecules) in terms of cost and stability[43,44]. In addition, previous studies have shown that spiro-OMeTAD-equipped carbon electrode-based perovskite solar cells offer lower efficiencies than a metal electrode-based device[45]. This is due to the incompatibility of some organic solvents in carbon paste with spiro-OMeTAD, which leads to its degradation[46]. Therefore, the effect of the inorganic CuSCN layer with excellent semiconducting properties such as high hole mobility, wide bandgap, optical transparency, thermal and chemical stability, and solution processability[44,47] on the performance of the device has been investigated. It should be noted that CuSCN can be deposited at low temperatures using various techniques including spin and spray coatings, doctor Blade, and electro-deposition[44,48–50].

Figure 6a shows the J–V characteristic calculated under AM 1.5G irradiation for the device comprised of FTO/TiO_2/Ag@SiO_2 NPs: $CH_3NH_3PbI_3$/CuSCN/Carbon. The optimized plasmonic cell in the absence of the hole transport layer of CuSCN delivers J_{sc} of 28.05 mA/cm^2, V_{oc} of 0.918 V, FF of 76.57%, and PCE of 19.72%.
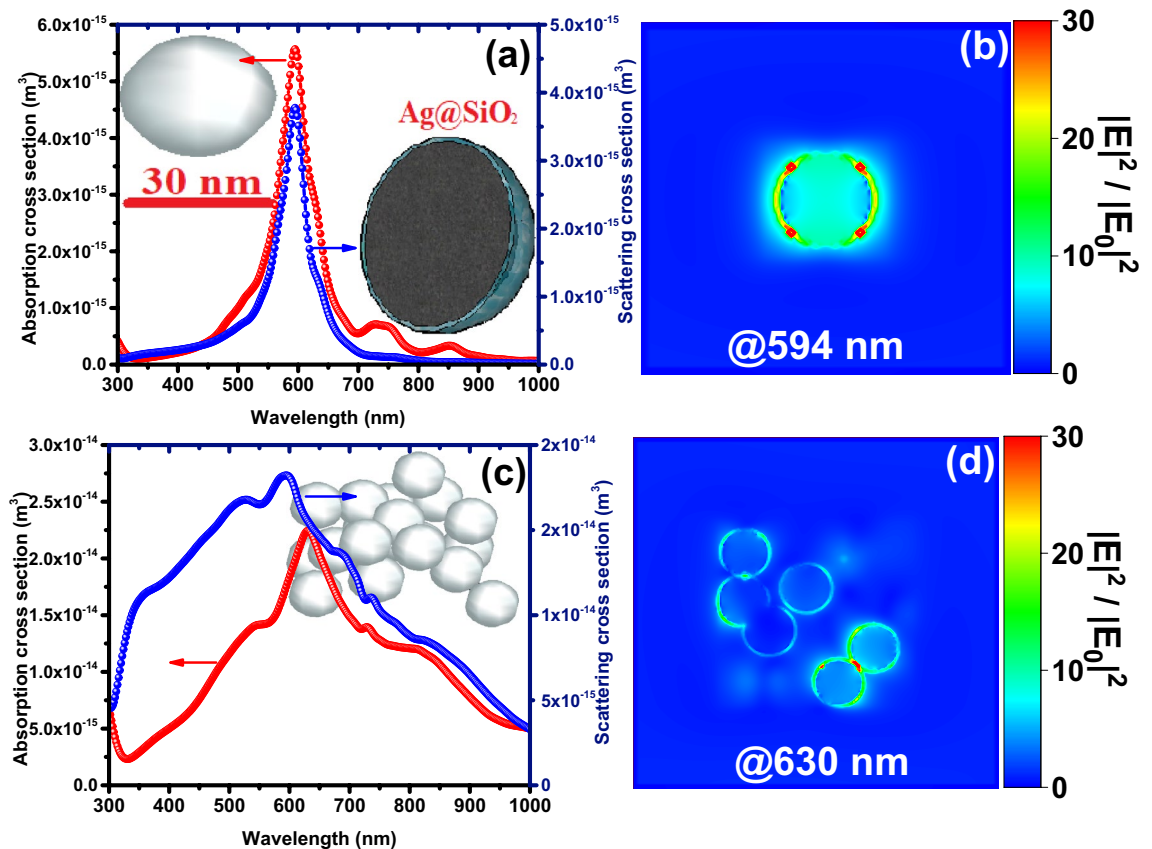
Figure 5. Absorption and scattering cross-sections (**a**, **c**) and near-field intensity enhancement (**b**, **d**) of (**a**, **b**) single and (**c**, **d**) a mass of 20 core–shell Ag@SiO₂ nanospheres (1 nm SiO₂ utter shell and total size of 32 nm).

On the other hand, the used solution-processed inorganic p-type CuSCN layer with a thickness of 30 nm at the perovskite-carbon interface has increased the device PCE by ~ 35% to 26.58% thanks to the increased V_{oc} and FF to 1.156 V and 81.64%, respectively (Table 3). The remarkable improvement of the V_{oc} is attributed to better interfacial energy alignment between the perovskite and CuSCN (see Figure S3). Figure 6b shows the recombination current density for the device equipped with a CuSCN layer compared to the reference device. Adding the CuSCN layer not only has reduced the SRH recombination by producing a back surface field and blocking electrons toward the TiO₂ ETL but also has reduced the current density of the back surface recombination down to ~ 10^{-22} mA/cm², even at high voltages, by appropriately aligning the interfacial energy.

Furthermore, Figs. 6c and d show the performance of the optimized plasmonic device as a function of the back contact work function. As the working function of the carbon electrode increases, which is possible by using suitable additives/binders in the carbon ink, V_{oc} and FF have increased thanks to the excellent alignment of the interfacial energy and the reduction of the recombination current density. As a result, a PCE above 26% is obtained for the work function of 5.4 eV (Table 3).

Conclusions

In summary, we have investigated the effects of the removal of mesoporous TiO₂, plasmonic nanoparticle embedding, and utilization of solution-processed inorganic p-type CuSCN as an HTL on the performance of carbon-based PSCs in an electro-optical study. We have shown that removing mesoporous TiO₂ can increase the device PCE by increasing the exciton generation rate and charge carriers' mobility in the vicinity of the CH₃NH₃PbI₃-compact TiO₂ interface. Furthermore, we have shown that the embedding of Ag@SiO₂ and SiO₂@Ag@SiO₂ plasmonic nanoparticles can increase the device PCE from 16.50% to 19.72% and 18.92% (in the optimum mass ratio), respectively, thanks to benefiting from the light scattering, trapping, and strong plasmonic fields produced by the nanoparticles. On the other hand, non-ideal carbon electrode has limited the device efficiency by increasing the interface recombination. Adding a solution-processed inorganic p-type CuSCN layer at the perovskite-carbon interface increased the device PCE to 26.58% by significantly improving the V_{oc} and FF thanks to the proper alignment of the interfacial energy and the reduction of the recombination current density. The same results were obtained by increasing the carbon working function (through incorporating suitable additives/binders to the carbon ink), and the cell PCE was enhanced up to 26% in the optimal case. These results pave the ways to achieve high efficiencies in carbon-based PSCs.
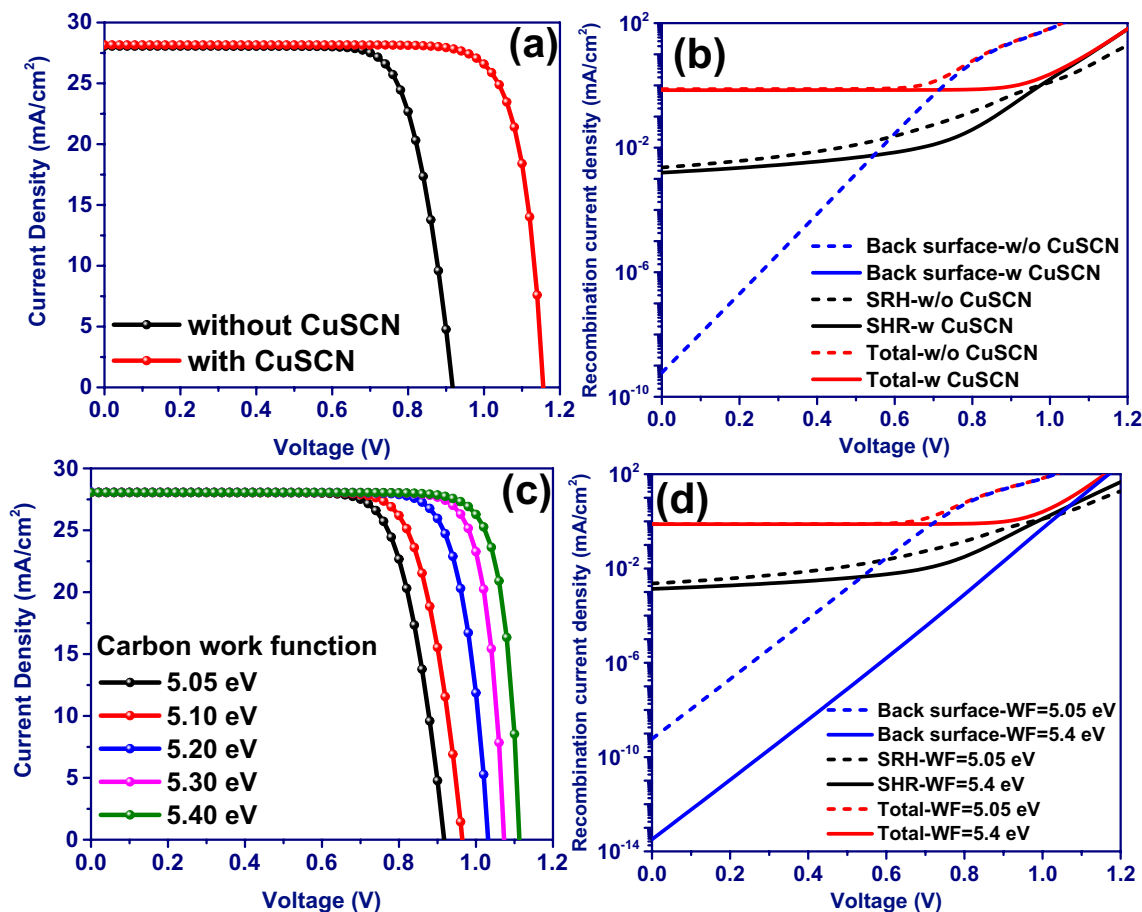
Figure 6. (**a**) J–V characteristics and (**b**) recombination current density of the optimized plasmonic device with and without the CuSCN hole transport layer. (**c**) J–V characteristics and (**d**) recombination current density of the optimized plasmonic device as a function of carbon electrode work function (WF).

Samples		J_{sc} (mA/cm^2)	V_{oc} (V)	FF (%)	PCE (%)
Adding HTL	Plasmonically optimized	28.05	0.918	76.57	19.72
	Adding CuSCN	28.16	1.156	81.64	26.58
Increasing Carbon work function	Plasmonically optimized (5.05)	28.05	0.918	76.57	19.72
	5.10 eV	28.05	0.964	77.61	20.99
	5.20 eV	28.05	1.032	81.34	23.55
	5.30 eV	28.05	1.074	84.27	25.39
	5.40 eV	28.05	1.113	84.44	26.36

Table 3. Electrical characteristics of the optimized plasmonic simulated device with and w/o the CuSCN hole transport layer and as a function of carbon electrode work function.

Materials and methods

Perovskite device fabrication. Firstly, a cleaned FTO glass substrate was treated in TiCl$_4$ (40 mM) at 70 °C for 30 min and washed with deionized water. Next, TiO$_2$ mesoporous scaffold has been prepared from the mixed TiO$_2$ precursor solution including Titanium(IV) ethoxide (Sigma-Aldrich, 12.7 g), concentrated HCl (Merck, 9.7 g), Pluronic P123 (Sigma-Aldrich, 4.0 g), and butyl alcohol (Sigma-Aldrich, 36.3 g). The solution has been dip-coated on the substrate (withdrawing speed; 30 mm/min) and has been subsequently annealed at 450 °C for 1 h. Then, the prepared PbI$_2$ solution (1.4 M) via solving PbI$_2$ in DMSO/DMF (1:9) has been spin-coated on TiO$_2$ mesoporous coated substrate at 2000 rpm for 20 s (during the process, the temperature is kept at 80 °C). To convert the PbI$_2$ film to CH$_3$NH$_3$PbI$_3$, CH$_3$NH$_3$I solution (1 mg mL^{-1}) was prepared in a mixed solvent of isopropanol/cyclohexane (1:9), and then, PbI$_2$ films were immersed into the CH$_3$NH$_3$I solution for 12 h, and the as-prepared methylammonium lead triiodide (MAPbI$_3$) films have been heated at 100 °C for 15 min[36,37]. Finally, a commercial carbon paste composed of carbon black and graphite has been used for preparing

the carbon back electrode. The carbon paste has been painted on the perovskite film followed by spraying an ethanol solution of 1H, 1H,2H,2H-perfluouorodecyltriethoxysilane (Sigma-Aldrich, 5% v/v) on the paste and heating at 100 °C for 1 h[7].

Numerical calculations. Optical-electrically coupled simulation regimes have been used to investigate the plasmonic nanoparticles embedding effects on the performance of carbon-based perovskite solar cells. The rate of exciton generation dependent on the absorption profile of the cell was calculated using FDTD software based on solving Maxwell equations[38]. The complex refractive indices obtained from the ellipsometric analyzes of the fabricated device were utilized to simulate and calculate the exciton generation rate profile optically. Perfectly matched layer (PML) boundary conditions are set at the top and bottom of the unit cell along the Z direction. Periodic boundary conditions are located along x and y directions. A plane wave light source propagated along the Z direction is used; the photon flux density is calculated based on standard solar spectrum AM1.5. Experimental data of the materials' complex refractive indices used for optical simulation are shown in Figure S1. To model the electrical response of the cell, the exciton generation rate profile is directly imported into the Solar Cell Capacitance Simulator (SCAPS-1D) software. Photovoltaic measurements of the fabricated devices were utilized to extract electrical parameters by fitting their corresponding *J–V* characteristics. The software uses the finite difference approach to solve electron and hole drift–diffusion equations to describe the motion of charge carriers inside the photoactive layer. Here Shockley–Read–Hall (SRH) model has been used to describe recombination current density[39]. The electrical parameters used for the simulation, which are extracted by fitting the simulation results with experimental data, are shown in Table S1.

References

1. Kojima, A., Teshima, K., Shirai, Y. & Miyasaka, T. Organometal halide perovskites as visible-light sensitizers for photovoltaic cells. *J. Am. Chem. Soc.* **131**, 6050–6051 (2009).
2. Jeong, M. *et al.* Stable perovskite solar cells with efficiency exceeding 24.8% and 0.3-V voltage loss. *Science (80-)* **369**, 1615–1620 (2020).
3. Domanski, K. *et al.* Not all that glitters is gold: Metal-migration-induced degradation in perovskite solar cells. *ACS Nano* **10**, 6306–6314 (2016).
4. Liang, L., Cai, Y., Li, X., Nazeeruddin, M. K. & Gao, P. All that glitters is not gold: Recent progress of alternative counter electrodes for perovskite solar cells. *Nano Energy* **52**, 211–238 (2018).
5. Mei, A. *et al.* A hole-conductor–free, fully printable mesoscopic perovskite solar cell with high stability. *Science (80-)* **345**, 295–298 (2014).
6. Chen, J. *et al.* Solvent effect on the hole-conductor-free fully printable perovskite solar cells. *Nano Energy* **27**, 130–137 (2016).
7. Keshavarzi, R., Molabahrami, N., Afzali, N. & Omrani, M. Improving efficiency and stability of carbon-based perovskite solar cells by a multifunctional triple-layer system: Anti-reflective, UV-protective, superhydrophobic and self-cleaning. *Sol. RRL* **4**, 202000491. https://doi.org/10.1002/solr.202000491 (2020).
8. Vijayaraghavan, S. N. *et al.* Low-temperature processed highly efficient hole transport layer free carbon-based planar perovskite solar cells with SnO2 quantum dot electron transport layer. *Mater. Today Phys.* **13**, 100204 (2020).
9. Zhang, X. *et al.* Efficient and carbon-based hole transport layer-free CsPbI 2 Br planar perovskite solar cells using PMMA modification. *J. Mater. Chem. C* **7**, 3852–3861 (2019).
10. Chen, R. *et al.* Carbon-based HTL-free modular perovskite solar cells with improved contact at perovskite/carbon interfaces. *J. Mater. Chem. C* **8**, 9262–9270 (2020).
11. Liang, L., Cai, Y. & Gao, P. A facile gas-driven ink spray (GDIS) deposition strategy toward hole-conductor-free carbon-based perovskite solar cells. *Emergent Mater.* https://doi.org/10.1007/s42247-021-00247-w (2021).
12. Cai, Y., Liang, L. & Gao, P. Promise of commercialization: Carbon materials for low-cost perovskite solar cells. *Chin. Phys. B* **27**, 018805 (2018).
13. Lee, K. *et al.* A highly stable and efficient carbon electrode-based perovskite solar cell achieved via interfacial growth of 2D PEA 2 PbI 4 perovskite. *J. Mater. Chem. A* **6**, 24560–24568 (2018).
14. Yang, Y. *et al.* Ultrasound-spray deposition of multi-walled carbon nanotubes on NiO nanoparticles-embedded perovskite layers for high-performance carbon-based perovskite solar cells. *Nano Energy* **42**, 322–333 (2017).
15. Abdi-Jalebi, M. *et al.* Maximizing and stabilizing luminescence from halide perovskites with potassium passivation. *Nature* **555**, 497–501 (2018).
16. Abdi-Jalebi, M. *et al.* Impact of a mesoporous titania–perovskite interface on the performance of hybrid organic–inorganic perovskite solar cells. *J. Phys. Chem. Lett.* **7**, 3264–3269 (2016).
17. Lu, H. *et al.* Efficient perovskite solar cells based on novel three-dimensional TiO2 network architectures. *Sci. Bull.* **61**, 778–786 (2016).
18. Calado, P. *et al.* Evidence for ion migration in hybrid perovskite solar cells with minimal hysteresis. *Nat. Commun.* **7**, 1–10 (2016).
19. Choi, J., Song, S., Hörantner, M. T., Snaith, H. J. & Park, T. Well-defined nanostructured, single-crystalline TiO2 electron transport layer for efficient planar perovskite solar cells. *ACS Nano* **10**, 6029–6036 (2016).
20. Omrani, M. K. & Fallah, H. Improving light trapping of polymer solar cell via doping a new array of triple core-shell spherical nanoparticles utilizing realistic modeling. *Sol. Energy* **163**, 600–609 (2018).
21. Omrani, M., Fallah, H. & Hajimahmoodzadeh, M. High efficiency metallic nanoshells for improving polymer solar cells performance: An opto-electrical study. *Sol. Energy* **207**, 409–418 (2020).
22. Cui, X. *et al.* Tailoring carrier dynamics in perovskite solar cells via precise dimension and architecture control and interfacial positioning of plasmonic nanoparticles. *Energy Environ. Sci.* **13**, 1743–1752 (2020).
23. Li, Y.-F., Kou, Z.-L., Feng, J. & Sun, H.-B. Plasmon-enhanced organic and perovskite solar cells with metal nanoparticles. *Nanophotonics* **9**, 3111–3133 (2020).
24. Gao, Y. *et al.* Plasmon-enhanced perovskite solar cells with efficiency beyond 21%: The asynchronous synergistic effect of water and gold nanorods. *ChemPlusChem* **86**, 291–297 (2021).

25. Zhao, D.-W. *et al.* Enhanced efficiency and stability of planar perovskite solar cells using a dual electron transport layer of gold nanoparticles embedded in anatase TiO2 films. *ACS Appl. Energy Mater.* **3**, 9568–9575 (2020).
26. Juan, F. *et al.* Plasmonic Au nanooctahedrons enhance light harvesting and photocarrier extraction in perovskite solar cell. *ACS Appl. Energy Mater.* **4**, 3201–3209 (2021).
27. Omrani, M., Mohammadi, H. & Fallah, H. Ultrahigh sensitive refractive index nanosensors based on nanoshells, nanocages and nanoframes: Effects of plasmon hybridization and restoring force. *Sci. Rep.* **11**, 2065 (2021).
28. Sovizi, M. & Omrani, M. K. Design and simulation of high sensitive cylindrical nanogear shell sensors according to localized surface plasmon resonance. *Optik (Stuttg).* **144**, 300–307 (2017).
29. Zhang, W. *et al.* Enhancement of perovskite-based solar cells employing core–shell metal nanoparticles. *Nano Lett.* **13**, 4505–4510 (2013).
30. Atwater, H. A. & Polman, A. Plasmonics for improved photovoltaic devices. *Nat. Mater.* **9**, 205–213 (2010).
31. Siavash Moakhar, R. *et al.* Recent advances in plasmonic perovskite solar cells. *Adv. Sci.* **7**, 1902448 (2020).
32. He, Z. *et al.* Influence of Ag@ SiO2 with Different Shell Thickness on Photoelectric Properties of Hole-Conductor-Free Perovskite Solar Cells. *Nanomaterials* **10**, 2364 (2020).
33. Lee, D. S. *et al.* Self-position of Au NPs in perovskite solar cells: Optical and electrical contribution. *ACS Appl. Mater. Interfaces* **8**, 449–454 (2016).
34. Dang, X. *et al.* Tunable localized surface plasmon-enabled broadband light-harvesting enhancement for high-efficiency panchromatic dye-sensitized solar cells. *Nano Lett.* **13**, 637–642 (2013).
35. Omrani, M., Fallah, H., Choy, K.-L. & Abdi-Jalebi, M. Impact of hybrid plasmonic nanoparticles on the charge carrier mobility of P3HT:PCBM polymer solar cells. *Sci. Rep.* **11**, 19774 (2021).
36. Chen, H. *et al.* Solvent engineering boosts the efficiency of paintable carbon-based perovskite solar cells to beyond 14%. *Adv. Energy Mater.* **6**, 1502087 (2016).
37. Chang, X. *et al.* Colloidal precursor-induced growth of ultra-even CH3NH3PbI3 for high-performance paintable carbon-based perovskite solar cells. *ACS Appl. Mater. Interfaces* **8**, 30184–30192 (2016).
38. OptiFDTD. http://www.optiwave.com/. OptiFDTD Software.
39. Burgelman, M., Nollet, P. & Degrave, S. Modelling polycrystalline semiconductor solar cells. *Thin Solid Films* **361**, 527–532 (2000).
40. Amini, M. *et al.* From dense blocking layers to different templated films in dye sensitized and perovskite solar cells: Toward light transmittance management and efficiency enhancement. *J. Mater. Chem. A* **6**, 2632–2642 (2018).
41. Yao, D. *et al.* Dimensionality-controlled surface passivation for enhancing performance and stability of perovskite solar cells via triethylenetetramine vapor. *ACS Appl. Mater. Interfaces* **12**, 6651–6661 (2020).
42. Yang, Y. *et al.* Ammonium-iodide-salt additives induced photovoltaic performance enhancement in one-step solution process for perovskite solar cells. *J. Alloys Compd.* **684**, 84–90 (2016).
43. Chen, W.-Y. *et al.* Low-cost solution-processed copper iodide as an alternative to PEDOT: PSS hole transport layer for efficient and stable inverted planar heterojunction perovskite solar cells. *J. Mater. Chem. A* **3**, 19353–19359 (2015).
44. Qin, P. *et al.* Inorganic hole conductor-based lead halide perovskite solar cells with 12.4% conversion efficiency. *Nat. Commun.* **5**, 1–6 (2014).
45. Yang, Y. *et al.* Spiro-OMeTAD or CuSCN as a preferable hole transport material for carbon-based planar perovskite solar cells. *J. Mater. Chem. A* **8**, 12723–12734 (2020).
46. Wei, H. *et al.* Free-standing flexible carbon electrode for highly efficient hole-conductor-free perovskite solar cells. *Carbon N. Y.* **93**, 861–868 (2015).
47. Wijeyasinghe, N. *et al.* Copper (I) thiocyanate (CuSCN) hole-transport layers processed from aqueous precursor solutions and their application in thin-film transistors and highly efficient organic and organometal halide perovskite solar cells. *Adv. Funct. Mater.* **27**, 1701818 (2017).
48. Murugadoss, G., Thangamuthu, R. & Kumar, S. M. S. Fabrication of CH3NH3PbI3 perovskite-based solar cells: Developing various new solvents for CuSCN hole transport material. *Sol. Energy Mater. Sol. Cells* **164**, 56–62 (2017).
49. Yang, I. S. *et al.* Formation of pristine CuSCN layer by spray deposition method for efficient perovskite solar cell with extended stability. *Nano Energy* **32**, 414–421 (2017).
50. Zhao, K. *et al.* Solution-processed inorganic copper (I) thiocyanate (CuSCN) hole transporting layers for efficient p–i–n perovskite solar cells. *J. Mater. Chem. A* **3**, 20554–20559 (2015).

Acknowledgements

Author contributions

M.K.O. Writing-Original Draft, Data analysis, Formal analysis, Validation, Methodology. R.K. Writing-Review & Editing, Validation, Data analysis. M.A.J. Writing-Review & Editing, Validation, Supervision. P.G. Writing-Review & Editing, Validation.

Competing interests

The authors declare no competing interests.

Additional information

Supplementary Information The online version contains supplementary material available at https://doi.org/10.1038/s41598-022-09284-9.

Correspondence and requests for materials should be addressed to M.O., R.K., M.A.-J. or P.G.

Reprints and permissions information is available at www.nature.com/reprints.

Publisher's note Springer Nature remains neutral with regard to jurisdictional claims in published maps and institutional affiliations.